JOURNAL OF SPACECRAFT AND ROCKETS
Vol. 34, No. 2, March–April 1997

Numerical Analysis of a Swept-Fin Missile

Kenneth J. Moran* and Philip S. Beran†
U.S. Air Force Institute of Technology, Wright–Patterson Air Force Base, Ohio 45433-7765

The flow about the complete Hypersonic Applied Research Technology missile is simulated for inviscid, laminar, and turbulent conditions and Mach numbers from 2 to 6. An explicit, second-order-accurate, flux-difference-splitting algorithm is implemented and employed to solve the Navier–Stokes equations. The equations are solved using a finite volume methodology. The formulation models turbulence with the zero-equation, Baldwin–Lomax turbulence model, accounting for pressure-gradient and compressibility effects. It is found that azimuthal clustering near the fins is crucial to predicting the pitching-moment coefficient at Mach numbers above 4. Static stability for laminar flow is found to improve very slightly over inviscid flow as Mach number increases. In the turbulent simulations, the structure of the flow near the fins is changed. In the fin region, the crossflow becomes blocked, and the turbulence causes bleeding around the fin leading edges. Ultimately, this results in lower fin effectiveness and reduced static stability.

Nomenclature

C_{m_α}	= pitching-moment coefficient
D	= diameter
E, F, G	= Cartesian flux components
$\hat{E}, \hat{F}, \hat{G}$	= numerical flux components
e_t	= total energy per unit volume
$\boldsymbol{F}$	= flux vector per unit area
L_ξ, L_η, L_ζ	= Strang operators
M_∞	= freestream Mach number
$\hat{\boldsymbol{n}}$	= unit normal vector
p	= pressure
q	= extrapolated quantity: density, pressure, velocity
q_x, q_y, q_z	= Cartesian heat flux components
$\hat{\boldsymbol{R}}$	= eigenvector of flux Jacobian
Re	= Reynolds number
S	= surface area
$S_x^\xi, S_y^\xi, S_z^\xi$	= Cartesian projections of a cell face area
t	= time
U	= dependent variables, conserved quantities
u, v, w	= Cartesian velocity components
V	= volume
y^+	= nondimensional boundary-layer distance
α	= angle of attack
γ	= ratio of specific heats
ρ	= density
$\tau_{xx}, \tau_{yy}, \tau_{zz}, \tau_{xy}, \tau_{xz}, \tau_{yz}$	= shear stresses
$\hat{\Phi}$	= characteristic-based dissipation term
ϕ	= azimuthal angle

Introduction

TO predict, substantiate, and understand the static-stability characteristics of a generic missile configuration at high Mach numbers, the Hypersonic Applied Research Technology (HART) missile was developed for experimental testing.[1] The model consisted of an ogive nose, cylindrical body, and one four-fin group located near the extreme aft end of the projectile (shown in Fig. 1 with a sharp nose tip and delta fins). The HART configuration was intended to provide the baseline characteristics of slender fin-stabilized bodies from low supersonic to hypersonic velocities.

Experimental testing of the HART missile began in 1987, and several empirical and inviscid computations have been performed.[1,2] To date, experimental, empirical, and inviscid computational analyses have had varying degrees of agreement.[1,2] In particular, the inviscid computational predictions of the pitching-moment coefficient from the ZEUS code[1] and the EAGLE code[2] differed significantly above Mach 4. The EAGLE solver computed a greater decrease in C_{m_α} with increasing M_∞ and much lower stability margins.[2]

The purpose of this study is to resolve the conflicts between previous computations and determine the true baseline static stability characteristics of the HART missile. Because of limitations in the experimental facility, the characteristics above Mach 4 must be obtained computationally. The disagreement between the ZEUS and EAGLE predictions is resolved in the current study using a new algorithm. This new algorithm is then used to obtain solutions for laminar and turbulent flow to evaluate the effects of viscosity and turbulence on the static stability of the HART missile.

In this study, computations are made for the HART missile with a sharp nose tip and clipped delta fins using the infinitely thin-fin approximation. A flux-difference-splitting algorithm is employed for the current calculations and was extensively validated for similar configurations where most grid refinement issues were addressed.[3] A grid refinement and sensitivity study is made to evaluate the variation of pitching moment with azimuthal grid spacing and the sensitivity of C_{m_α} to α. Numerical experiments are then undertaken to determine the aerodynamic coefficients of the HART missile. Parametric Mach number studies ($M_\infty = 2-6$) are conducted for $\alpha = 0$ and 5 deg under inviscid, laminar, and turbulent conditions. Static stability is investigated over the Mach range with the emphasis on the trend above Mach 4 (i.e., whether the HART configuration is statically stable between Mach 4 and 6).

The quality of the infinitely thin fin was examined by the first author.[4] For the flight conditions of interest in this study, fin thickness was found not to significantly alter the flow structure or C_{m_α} behavior with change in Mach number.

Analysis Methodology

Description of Grid

A two-dimensional C grid is constructed and then rotated about the body centerline to produce a three-dimensional grid. In this way, each plane is normal to the missile body, and the fins coincide with distinct grid planes. The two-dimensional C grid is constructed such that a cell center slightly displaced from the axisymmetry line is mirrored by one displaced exactly the same amount, but azimuthally located 180 deg apart. Grid spacing in the streamwise and normal directions is based on the validations of the current algorithm for similar configurations at Mach numbers from 2 to 8 in Ref. 4. The two-dimensional grid is body conforming with ξ grid lines normal to the missile surface and η grid lines normal to the symmetry line.

The nose tip is very slightly rounded to more accurately represent the experimental model and enable the bow shock to be captured a small distance away from the surface. The modified nose is

Received Aug. 2, 1995; revision received Sept. 3, 1996; accepted for publication Oct. 5, 1996.

*Ph.D. Graduate, Department of Aeronautics and Astronautics, Graduate School of Engineering; also Major, U.S. Air Force. Member AIAA.

†Associate Professor, Department of Aeronautics and Astronautics, Graduate School of Engineering. Senior Member AIAA.

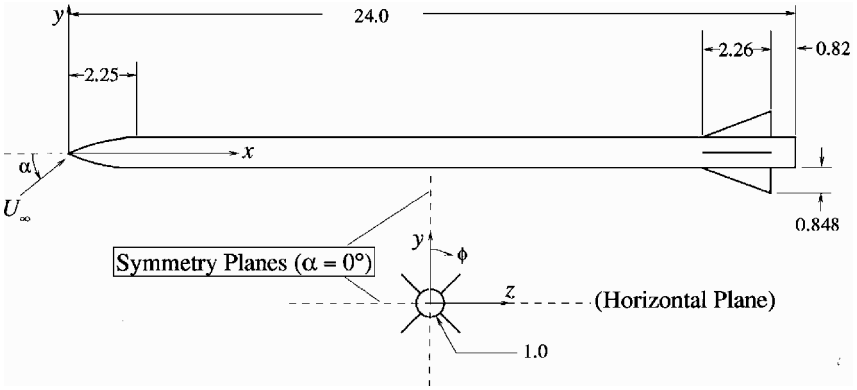

Fig. 1 HART baseline model.

spherically rounded with $R_n/R_b = 0.05$. Dolling and Gray[5] found that surface pressure (away from the tip) and boundary-layer development are virtually unaffected by this level of blunting.

Governing Equations

The integral form of the Navier–Stokes equations is written as

$$\frac{\mathrm{d}}{\mathrm{d}t}\int_V U\,\mathrm{d}V + \oint_S \hat{\boldsymbol{n}}\cdot\boldsymbol{F}\,\mathrm{d}S = 0 \tag{1}$$

The volume of the region over which Eq. (1) is applied is V, and the bounding surface of that region is S.

The nondimensional flux definitions in each Cartesian direction are[6]

$$\hat{\boldsymbol{n}}_x\cdot\boldsymbol{F} = E =$$

$$\begin{bmatrix} \rho u \\ \rho u^2 + p - Re^{-1}\tau_{xx} \\ \rho uv - Re^{-1}\tau_{xy} \\ \rho uw - Re^{-1}\tau_{xz} \\ (e_t + p)u - Re^{-1}\left(u\tau_{xx} + v\tau_{xy} + w\tau_{xz} - \dfrac{q_x}{(\gamma-1)M_\infty^2}\right) \end{bmatrix}$$

$$\hat{\boldsymbol{n}}_y\cdot\boldsymbol{F} = F =$$

$$\begin{bmatrix} \rho v \\ \rho uv - Re^{-1}\tau_{xy} \\ \rho v^2 + p - Re^{-1}\tau_{yy} \\ \rho vw - Re^{-1}\tau_{yz} \\ (e_t + p)v - Re^{-1}\left(u\tau_{xy} + v\tau_{yy} + w\tau_{yz} - \dfrac{q_y}{(\gamma-1)M_\infty^2}\right) \end{bmatrix}$$

$$\hat{\boldsymbol{n}}_z\cdot\boldsymbol{F} = G =$$

$$\begin{bmatrix} \rho w \\ \rho uw - Re^{-1}\tau_{xz} \\ \rho vw - Re^{-1}\tau_{yz} \\ \rho w^2 + p - Re^{-1}\tau_{zz} \\ (e_t + p)w - Re^{-1}\left(u\tau_{xz} + v\tau_{yz} + w\tau_{zz} - \dfrac{q_z}{(\gamma-1)M_\infty^2}\right) \end{bmatrix} \tag{2}$$

The equation of state for a perfect gas defines pressure. The viscous stresses and heat-flux vector can be found in Ref. 6. For inviscid calculations, those terms preceded by Re^{-1} are set to zero. For laminar viscous computations, μ is determined using Sutherland's formula.[6] For turbulent flow, eddy viscosity μ_t is invoked to achieve closure.[7]

Turbulence Modeling

A location is selected along the missile length to separate laminar and turbulent portions of the boundary layer; a fully turbulent condition is assumed for the wake region. Eddy viscosity μ_t is calculated only in the turbulent regions. The point designated to delineate the laminar and turbulent regions is selected on the ogive nose at $x/D = 1.25$ based on experimental evidence.[2] The Baldwin–Lomax algebraic model[8] is used to compute μ_t on the turbulent portion of the forebody because of its relatively low computational cost and ease of application. An empirical model is used to calculate μ_t in the wake. The implementation of the Baldwin–Lomax model and the empirical wake model with the current numerical algorithm was extensively validated for finless missile configurations in Ref. 9. The choice of a zero-equation turbulence model is appropriate for the flight conditions under investigation. The flow remains attached, and no vortical structures develop.

General Algorithm Description

The Navier–Stokes equations (Reynolds averaged for turbulent flows) are solved with an explicit, time-integration technique, incorporating an upwind, Roe type, flux-difference-splitting (FDS) formulation based on the work of Refs. 10 and 11. In the FDS method, the convective terms are modified in an upwind manner, and the viscous terms are centrally differenced. The modified convective fluxes are approximations to average fluxes at cell interfaces and, as such, are often called numerical fluxes. In addition, the modification is second-order preserving for those interfaces located away from extrema (e.g., shocks). The current scheme uses the non-MUSCL technique to determine the numerical fluxes at cell interfaces.[11] The flux in the ξ-coordinate direction at the $(i+\frac{1}{2}, j, k)$ interface is, therefore, approximated by

$$\begin{aligned}\hat{E}_{i+\frac{1}{2}jk} \equiv \tfrac{1}{2}\Big[&\left(S_x^\xi\right)_{i+\frac{1}{2}jk}(E_{i+1jk} + E_{ijk}) + \left(S_y^\xi\right)_{i+\frac{1}{2}jk} \\ &\times (F_{i+1jk} + F_{ijk}) + \left(S_z^\xi\right)_{i+\frac{1}{2}jk}(G_{i+1jk} + G_{ijk}) \\ &+ \tfrac{1}{2}(V_{i+1jk} + V_{ijk})\hat{R}_{i+\frac{1}{2}jk}\hat{\Phi}_{i+\frac{1}{2}jk}\Big]\end{aligned} \tag{3}$$

The addition of the last term in Eq. (3) is a modification to Roe's first-order, FDS algorithm.[12] For Roe's scheme, $\hat{\Phi}$ is composed of eigenvalues and characteristic variables and simply acts as an upwinding term. Because of the work of Harten and Yee, $\hat{\Phi}$ also acts to limit the characteristic variables, thereby providing higher accuracy.[10,11] This is done in the current study with the minmod limiter; details regarding the development and implementation of the limiter are contained in Ref. 4. Explicit forms for $\hat{\boldsymbol{R}}$ and $\hat{\Phi}$ are also set forth in Ref. 4. The other interfaces have numerical fluxes with similar construction.

Equation (1) is then written as

$$\begin{aligned}U_{ijk}^{n+1} = U_{ijk}^n - \frac{\Delta t}{V_{ijk}}\Big[&\hat{E}^n_{i+\frac{1}{2}jk} - \hat{E}^n_{i-\frac{1}{2}jk} + \hat{F}^n_{ij+\frac{1}{2}k} \\ &- \hat{F}^n_{ij-\frac{1}{2}k} + \hat{G}^n_{ijk+\frac{1}{2}} - \hat{G}^n_{ijk-\frac{1}{2}}\Big]\end{aligned} \tag{4}$$

The scheme is implemented as a set of one-dimensional operators utilizing the Strang-type fractional-step[11] method to ensure that second-order spatial accuracy is preserved:

$$U^{n+2}_{ijk} = L^{h/2}_{\eta} L^{h}_{\xi} L^{h}_{\zeta} L^{h}_{\eta} L^{h}_{\zeta} L^{h}_{\xi} L^{h/2}_{\eta} U^{n}_{ijk} \tag{5}$$

where

$$\begin{aligned} L^{h/2}_{\eta} U^{n}_{ijk} &= U^{*}_{ijk} = U^{n}_{ijk} - \frac{\Delta t}{2V_{ijk}} \left(\hat{F}^{n}_{ij+\frac{1}{2}k} - \hat{F}^{n}_{ij-\frac{1}{2}k} \right) \\ L^{h}_{\xi} U^{*}_{ijk} &= U^{**}_{ijk} = U^{*}_{ijk} - \frac{\Delta t}{V_{ijk}} \left(\hat{E}^{*}_{i+\frac{1}{2}jk} - \hat{E}^{*}_{i-\frac{1}{2}jk} \right) \\ L^{h}_{\zeta} U^{**}_{ijk} &= U^{***}_{ijk} = U^{**}_{ijk} - \frac{\Delta t}{V_{ijk}} \left(\hat{G}^{**}_{ijk+\frac{1}{2}} - \hat{G}^{**}_{ijk-\frac{1}{2}} \right) \end{aligned} \tag{6}$$

Application of the entire sequence of operators advances the solution two time levels.

Table 1 Summary of numerical experiments for sharp nose tip model, without base region

Case	M_∞	α	$I \times J \times K$	$(\Delta r/D)\|_{\text{body}}$
		Inviscid (coarse grid)		
S1	2.0	0	61 × 81 × 33	0.001
S2	3.0	0	61 × 81 × 33	0.001
S3	3.5	0	61 × 81 × 33	0.001
S4	4.5	0	61 × 81 × 33	0.001
S5	6.0	0	61 × 81 × 33	0.001
S6	2.0	5	61 × 81 × 33	0.001
S7	3.0	5	61 × 81 × 33	0.001
S8	3.5	5	61 × 81 × 33	0.001
S9	4.5	5	61 × 81 × 33	0.001
S10	6.0	5	61 × 81 × 33	0.001
		Laminar (coarse grid)		
S11	2.0	0	61 × 81 × 33	0.001
S12	3.0	0	61 × 81 × 33	0.001
S13	3.5	0	61 × 81 × 33	0.001
S14	4.5	0	61 × 81 × 33	0.001
S15	6.0	0	61 × 81 × 33	0.001
S16	2.0	5	61 × 81 × 33	0.001
S17	3.0	5	61 × 81 × 33	0.001
S18	3.5	5	61 × 81 × 33	0.001
S19	4.5	5	61 × 81 × 33	0.001
S20	6.0	5	61 × 81 × 33	0.001
		Laminar (fine grid)		
S21	2.0	0	61 × 101 × 33	0.000025
S22	3.5	0	61 × 101 × 33	0.000025
		Turbulent (coarse grid)		
S23	2.0	0	61 × 81 × 33	0.001
S24	3.0	0	61 × 81 × 33	0.001
S25	3.5	0	61 × 81 × 33	0.001
S26	4.5	0	61 × 81 × 33	0.001
S27	6.0	0	61 × 81 × 33	0.001
S28	2.0	5	61 × 81 × 33	0.001
S29	3.0	5	61 × 81 × 33	0.001
S30	3.5	5	61 × 81 × 33	0.001
S31	4.5	5	61 × 81 × 33	0.001
S32	6.0	5	61 × 81 × 33	0.001
		Turbulent (fine grid)		
S33	2.0	0	61 × 101 × 33	0.000025
S34	3.5	0	61 × 101 × 33	0.000025

Boundary Conditions

Because of the supersonic condition at both the inflow and outflow boundaries, the associated boundary conditions are relatively straightforward; at the inflow, freestream conditions are applied, and at the outflow, extrapolation is employed. For the body, base, and fin surfaces, impermeability or no slip (viscous only) are enforced. Also, on solid surfaces a vanishing pressure gradient and a vanishing density gradient or an adiabatic wall (viscous only) are enforced. Because the HART missile is bisymmetric, and the model was inclined within one of the planes of symmetry, calculations were made around only half the circumference of the missile. Symmetry is then enforced at the azimuthal boundaries. For $\alpha = 0$, axisymmetry is applied at the singular line boundary. When $\alpha \neq 0$, the following extrapolation is used to determine density, pressure, and each velocity component at the singular line:

$$q_1 = 3q_2 - 3q_3 + q_4 \tag{7}$$

Equation (7) was developed in Ref. 4; subscripts 1 and 2 refer to the two cell centers nearest the symmetry line.

Results

The case history of calculations made to assess the aerodynamics of the HART missile is tabulated in Table 1. The Mach number is varied from 2 to 6, and calculations are made at $\alpha = 0$ and 5 deg for inviscid, laminar, and turbulent flowfield conditions. A limited number of computations are performed with refined spacing near the missile body (cases S21, S22, S33, and S34). The spacing near the missile body for these cases is equivalent to $y^+ \approx 1$. Because of limited resources, computations with the refined grid are done for only two Mach numbers. Cases S11, S12, S16, and S17 were computed by Blake[13] as part of an M.S. thesis involving parallel computing techniques. Blake used the present algorithm to make those computations.

Table 2 lists the computations made to assess two sensitivity issues. The grid dimensions (I, J, and K) refer to axial, radial, and azimuthal dimensions, respectively. Cases R1–R4 vary the angular spacing ($\Delta\phi$) near the fin to determine the sensitivity of the pitching-moment coefficient. The spacing is varied from approximately 6 to 0.5 deg. In addition, the angle of attack is varied from 5 to 0.5 deg (cases R4–R6) to determine the variation of C_{m_α} with α. All sensitivity calculations are conducted at $M_\infty = 3.5$ on a highly blunted HART variation.

The pitching-moment coefficient C_{m_α} shows some sensitivity to angular spacing. Figure 2 demonstrates that C_{m_α} is influenced significantly by the angular spacing near the fins. As $\Delta\phi$ decreases from 6 to 0.5 deg, C_{m_α} decreases (more negative) about 30%. In addition, C_{m_α} appears to be approaching an asymptotic value near 0.5 deg. Throughout the rest of this study, results are presented for nodes clustered near the fins.

The rate at which the pitching moment vanishes as $\alpha \to 0$ is shown in Fig. 3. As the angle of attack increases, the pitching-moment coefficient changes only slightly. The three values of C_{m_α} plotted in Fig. 3 differ by about 1%. Unfortunately, resource limitations prevent this analysis from being repeated at other Mach numbers. However, the results at $M_\infty = 3.5$ agree with inviscid linear theory,[14] which indicates that C_{m_α} is independent of α. An angle of attack of 5 deg is representative of the experiments and is selected in the current study for all remaining computations performed with a nonzero angle of attack.

The inviscid pitching-moment results are primarily compared with previous inviscid results from EAGLE. Comparisons are also

Table 2 Summary of numerical experiments used for grid sensitivity analysis (blunt nose tip model)

Case	M_∞	α	$I \times J \times K$	$\Delta\phi_{\min}$	$\Delta\phi_{\max}$	$(\Delta r/D)\|_{\text{body}}$	Description
R1	3.5	5.0	61 × 81 × 33	5.6250	5.6250	0.001	Laminar, uniform $\Delta\phi$
R2	3.5	5.0	61 × 81 × 65	2.8125	2.8125	0.001	Laminar, uniform $\Delta\phi$
R3	3.5	5.0	61 × 81 × 105	1.7308	1.7308	0.001	Laminar, uniform $\Delta\phi$
R4	3.5	5.0	61 × 81 × 33	0.5000	15.5000	0.001	Laminar, clustered $\Delta\phi$
R5	3.5	2.5	61 × 81 × 33	0.5000	15.5000	0.001	Laminar, clustered $\Delta\phi$
R6	3.5	0.5	61 × 81 × 33	0.5000	15.5000	0.001	Laminar, clustered $\Delta\phi$

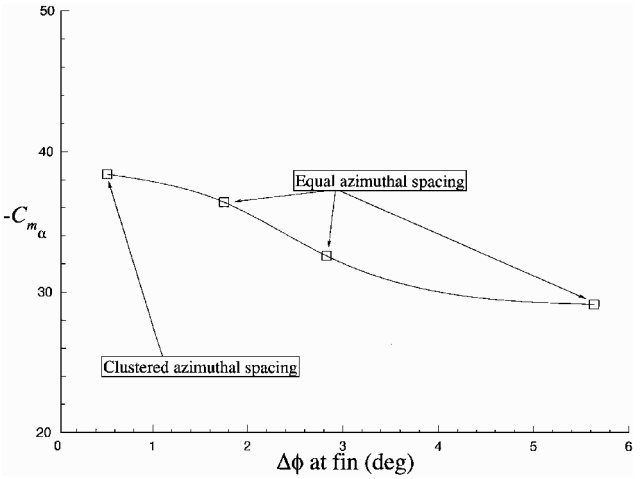

Fig. 2 Pitching-moment coefficient sensitivity to angular spacing near the fin.

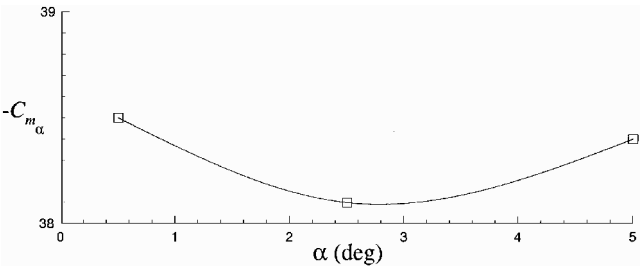

Fig. 3 Pitching-moment coefficient sensitivity to angle of attack.

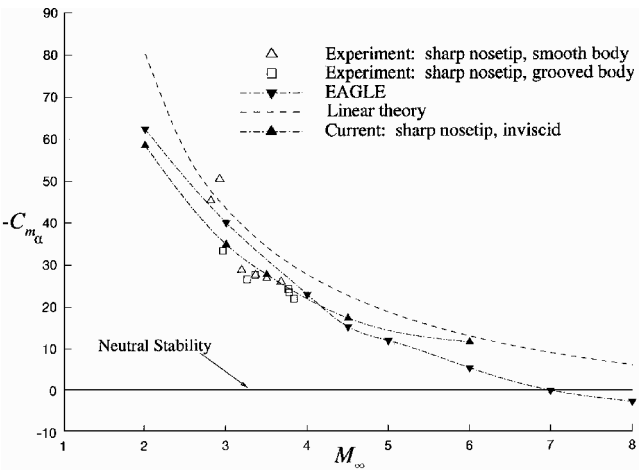

Fig. 4 Pitching-moment coefficient for clipped-delta-fin model.

made to the experimental data to confirm the trends of C_{m_α} with M_∞ at lower Mach numbers. The EAGLE results are shown with the experimental data and the current inviscid results (cases S1–S10) in Fig. 4. The Ballistic Gun Range Facility limits the experimental data testing to Mach numbers below 4.5 (Ref. 1). Experimental data between Mach 3.9 and 4.5 are not shown in either figure because of possible experimental model variations.[4]

In contrast to the EAGLE results, the current results show a much gentler decrease in the stability margin as Mach number increases beyond 4. Although free-flight data are unreliable for $M_\infty > 3.9$, available data above Mach 3 also appear to exhibit a more modest decline in C_{m_α}. The difference between the values predicted by the EAGLE solver and those predicted by the current solver are very important because neutral stability is reached at $M_\infty = 7$ with EAGLE. The authors believe the difference is related to the azimuthal clustering of nodes in the present study vs coarse unclustered nodes in the EAGLE study. In this study, coarse unclustered azimuthal grid spacing underpredicted the stability coefficient by over 20%.

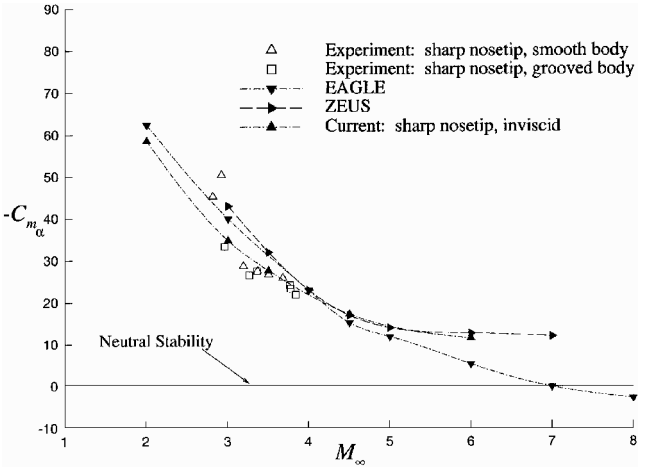

Fig. 5 Comparison of pitching-moment coefficient from three inviscid solvers.

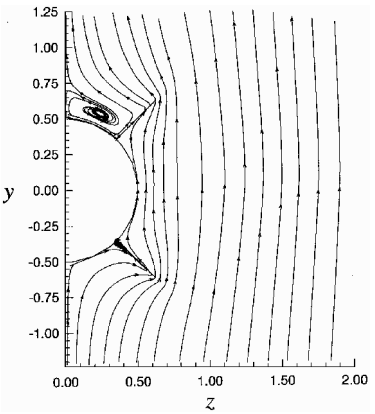

Fig. 6 Cross-plane streamlines, case S6: $M_\infty = 2$ and $\alpha = 5$ deg.

In Fig. 5, the C_{m_α}–M_∞ trends for all inviscid computations (prior and present) on the sharp nose tip model are compared. The experimental data are included for reference. The ZEUS results from the baseline delta-fin configuration are included to provide useful qualitative information at higher Mach numbers. Above Mach 4, the present computations depict a trend with Mach number that is similar to that predicted by ZEUS. Again, the difference in the EAGLE predictions is believed to be related to azimuthal clustering near the fin surfaces.

The crossplane velocity components are shown in Fig. 6 for inviscid flow at $M_\infty = 2$ and $\alpha = 5$ deg (case S6). Streamlines created from the crossplane velocities are also shown in Fig. 6. The shape of the streamline, which begins on the windside of the missile near the symmetry plane ($y = -1.25$, $z = 0$), shows that the crossflow is not significantly displaced from the missile surface (expect for the region above the leeside fin). In addition, the velocity vectors show that the crossflow is small, and the expansion and compression on each fin are distinctly separated.

The effects of viscosity are initially assessed for laminar boundary-layer conditions. Most experiments indicate that the boundary layer becomes turbulent upstream of the fins, but the impact of turbulence is best determined after laminar results are documented. Again, pitching-moment coefficients from the present study are plotted vs Mach number with the experimental data (Fig. 7). The inviscid results that were previously discussed are included for reference. Interestingly, the laminar and inviscid results agree at low Mach numbers, and begin to diverge at about $M_\infty = 3.5$. At the higher Mach numbers, the boundary layer appears to improve C_{m_α} (i.e., C_{m_α} is more negative).

The pressure contours in the crossplane (y–z plane) for laminar flow and $\alpha = 5$ deg at $M_\infty = 2$ and 6 (cases S16 and S20) are compared to those for inviscid flow (cases S6 and S10) in Figs. 8 and 9. These crossplane contour plots are for $x/D = 21.8$, an axial station near the middle of the fins.

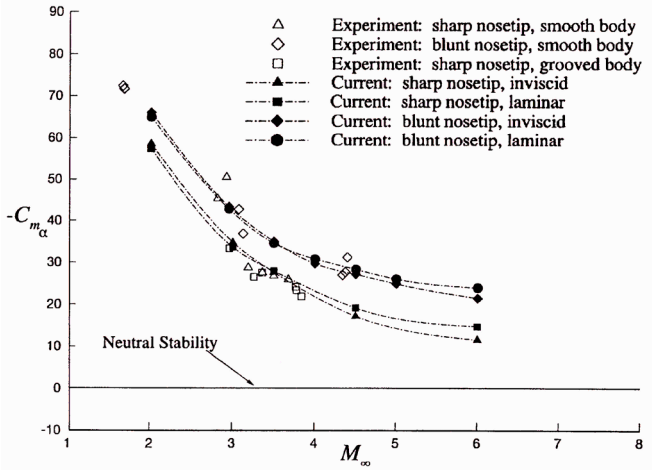

Fig. 7 Pitching-moment coefficient for clipped-delta-fin model at inviscid and laminar conditions.

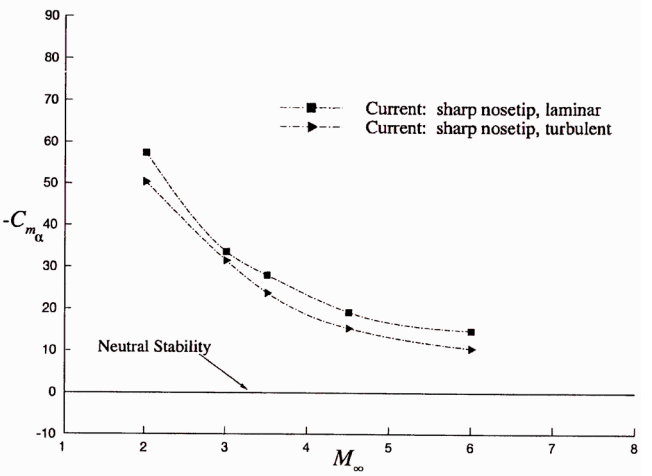

Fig. 10 Pitching-moment coefficient for clipped-delta-fin model at laminar and turbulent conditions.

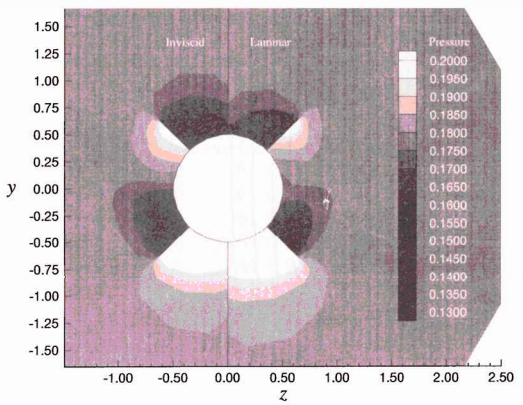

Fig. 8 Pressure contours for inviscid and laminar flow: $M_\infty = 2$ and $\alpha = 5$ deg.

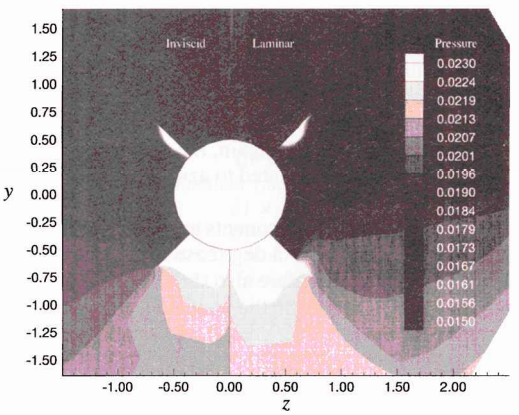

Fig. 9 Pressure contours for inviscid and laminar flow: $M_\infty = 6$ and $\alpha = 5$ deg.

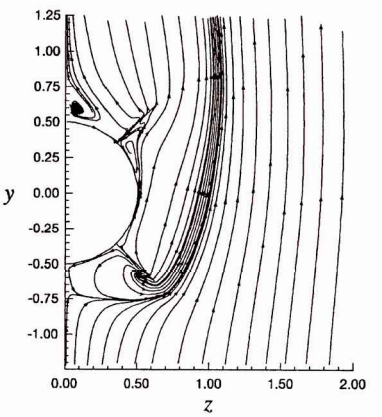

Fig. 11 Cross-plane streamlines, case S28: $M_\infty = 2$ and $\alpha = 5$ deg.

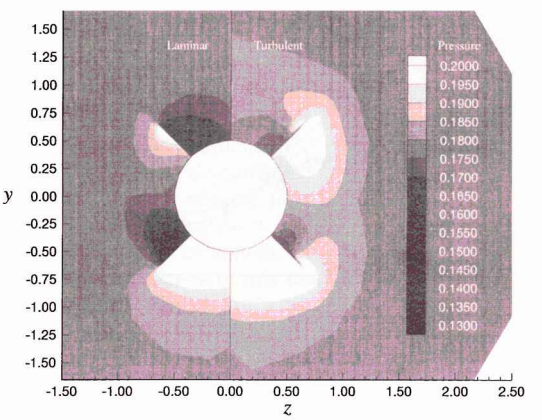

Fig. 12 Pressure contours for laminar and turbulent flow: $M_\infty = 2$ and $\alpha = 5$ deg.

As M_∞ increases, the pressure gradient near the fin surfaces increases. This is evidenced by the piling up of pressure contours on the bottom of the leeside fin, further demonstrating that grid refinement normal to the fins is needed.

The crossplane pressure contours in Fig. 8 also indicate that the laminar flow structure is similar to the inviscid structure at Mach 2, which supports the stability coefficient results in Fig. 7. At higher Mach numbers, however, the boundary layer has influenced the pressure distribution slightly. The higher pressure values on the compression sides of the fins for $M_\infty = 6$ can be seen in Fig. 9. Therefore, as Mach number increases, the presence of viscosity causes less decrease in the pitching-moment coefficient (as seen in Fig. 7).

The influence of turbulence is now addressed. The turbulent results are plotted with the laminar results in Fig. 10. The pitching-moment coefficient for turbulent flow changes measurably over that for laminar flow. The lower static stability (C_{m_α} less negative) for the turbulent computations is due to the compression bleeding around the leading edge of the windside fin, which affects the pressure on the expansion side of the fin. The phenomenon of bleeding is seen in the streamlines of the crossplane velocity components (Fig. 11). The presence of turbulence creates a large region for which the crossflow is blocked. Consequently, the oncoming crossplane streamlines are significantly displaced from the missile body, allowing for a reduced level of expansion around the leading edge of the windside fin.

The bleeding effect for turbulent flow is also seen in the crossplane pressure contours. The crossplane pressure contours for turbulent flow, $\alpha = 5$ deg and $M_\infty = 2$ (case S28), are compared to those from laminar flow in Fig. 12. The bleeding of higher pressures around the fin leading edges is visible in the turbulent case.

Conclusions

Using the present developed technique, the flow about the complete HART missile configuration is simulated. As expected, pitching moment is dominated by compressibility effects because fin effectiveness is seen to decrease with increasing Mach number. The aerodynamic characteristics of the HART missile are predicted at Mach numbers beyond the experimental testing capabilities. The current simulations predict the HART configuration to be statically stable through Mach 6.

The current predictions also indicate that C_{m_α} decreases with increasing Mach number much less than the previous EAGLE computations. The differences in C_{m_α} between the current inviscid results and EAGLE results above $M_\infty = 4$ suggest that the clustering of nodes near the fin surfaces is very important as Mach number increases. In this study, large azimuthal grid spacing near fin surfaces underpredicted the stability coefficient by over 20%.

For laminar flow, the boundary layer has influenced the pressure distribution slightly. As Mach number increases, the presence of viscosity causes less decrease in the pitching-moment coefficient.

The presence of turbulence is found to be significant. The expansion and compression associated with the upper and lower surfaces of the inclined fins produce less net lift for the present turbulent computations than the present inviscid or laminar computations. In the fin region, the crossflow becomes blocked, and the turbulence causes bleeding around the fin leading edges. Ultimately, this results in lower fin effectiveness and reduced static stability. These zero-equation turbulence model results could serve as a baseline for results using other turbulence models.

Acknowledgments

The authors are very grateful to Bruce Simpson for many helpful discussions throughout the course of this work, as well as valuable computing resources on the Cray Y-MP8 at Eglin Air Force Base, Florida. Computational resources for this work were also provided by the Department of Defense High Performance Computing Program through access to the Cray Y-MP8 and Cray C-916 at Vicksburg, Mississippi, and the Ohio Supercomputing Center through access to the Cray Y-MP8 at Ohio State University.

References

[1]Gates, R. S., Winchenbach, G. L., and Cipolla, J. R., "Aerodynamic Test and Analysis of a Slender Generic Missile Configuration," *Proceedings of the AIAA Atmospheric Flight Mechanics Conference* (Boston, MA), AIAA, Washington, DC, 1989, pp. 192–200 (AIAA Paper 89-3368).

[2]Vitale, H. E., Winchenbach, G. L., and Riner, W. C., "Aerodynamic Test and Ongoing Analysis of a Slender Generic Missile Configuration," *Proceedings of the AIAA Atmospheric Flight Mechanics Conference* (New Orleans, LA), AIAA, Washington, DC, 1991, pp. 432–438 (AIAA Paper 91-2895).

[3]Moran, K. J., and Beran, P. S., "Navier–Stokes Simulations of Slender Axisymmetric Shapes in Supersonic, Turbulent Flow," *AIAA Journal*, Vol. 32, No. 7, 1994, pp. 1446–1456.

[4]Moran, K. J., "An Aerodynamic and Static-Stability Analysis of the Hypersonic Applied Research Technology (HART) Missile," Ph.D. Dissertation, Graduate School of Engineering, U.S. Air Force Inst. of Technology, Wright–Patterson AFB, OH, April 1994.

[5]Dolling, D. S., and Gray, W. K., "Experimental Study of Supersonic Turbulent Flow on a Blunted Axisymmetric Body," *AIAA Journal*, Vol. 24, No. 5, 1986, pp. 793–799.

[6]Anderson, D. A., Tannehill, J. C., and Pletcher, R. H., *Computational Fluid Mechanics and Heat Transfer*, 1st ed., Hemisphere, New York, 1984, pp. 181, 208.

[7]White, F. M., *Viscous Fluid Flow*, 2nd ed., McGraw–Hill, New York, 1991, pp. 437–443.

[8]Baldwin, B. S., and Lomax. H., "Thin Layer Approximation and Algebraic Model for Separated Turbulent Flow," AIAA Paper 78-0257, Jan. 1978.

[9]Moran, K. J., and Beran, P. S., "Fin-Interference Effects on the Aerodynamics of a Swept-Fin Missile," *Proceedings of the AIAA 13th Applied Aerodynamics Conference* (San Diego, CA), AIAA, Washington, DC, 1995, pp. 1111–1128 (AIAA Paper 95-1899).

[10]Harten, A., "High Resolution Schemes for Hyperbolic Conservation Laws," *Journal of Computational Physics*, Vol. 49, March 1983, pp. 357–393.

[11]Yee, H. C., "A Class of High-Resolution Explicit and Implicit Shock-Capturing Methods," NASA TM 101088, Feb. 1989.

[12]Roe, P. L., "Approximate Riemann Solvers, Parameter Vectors, and Difference Schemes," *Journal of Computational Physics*, Vol. 43, Oct. 1981, pp. 357–372.

[13]Blake, D. J., "A Numerical Study of High-Speed Missile Configurations Using a Block-Structured Parallel Algorithm," M.S. Thesis, Graduate School of Engineering, U.S. Air Force Inst. of Technology, AFIT/GAE/ENY/93D-07, Wright–Patterson AFB, OH, Dec. 1993.

[14]Ashley, H., and Landahl, M., *Aerodynamics of Wings and Bodies*, 1st ed., Dover, New York, 1965, pp. 81–123.

R. M. Cummings
Associate Editor